Published in final edited form as:
Neuroimage. 2012 May 15; 61(1): 304–313. doi:10.1016/j.neuroimage.2012.01.115.

Multi-projection magnetic resonance inverse imaging of the human visuomotor system

Kevin Wen-Kai Tsai[1], **Aapo Nummenmaa**[2,3], **Thomas Witzel**[3], **Wei-Tang Chang**[3], **Wen-Jui Kuo**, and **Fa-Hsuan Lin**[1,3,*]

[1]Institute of Biomedical Engineering, National Taiwan University, Taipei, Taiwan [2]Department of Biomedical Engineering and Computational Science, Aalto University, Espoo, Finland [3]MGH-HST Athinoula A. Martinos Center for Biomedical Imaging, Charlestown, MA, USA [4]Institute of Neuroscience, National Yang-Ming University, Taipei, Taiwan

Abstract

Using highly parallel radiofrequency (RF) detection, magnetic resonance inverse imaging (InI) can achieve 100 ms temporal resolution with whole brain coverage. This is achieved by trading off partition encoding steps and thus spatial resolution for a higher acquisition rate. The reduced spatial information is estimated by solving under-determined inverse problems using RF coil sensitivity information. Here we propose multi projection inverse imaging (mInI) to combine different projection images to improve the spatial resolution of InI. Specifically, coronal, sagittal, and transverse projection images were acquired from different runs of the fMRI acquisitions using a 32-channel head coil array. Simulations show that mInI improves the quality of the instantaneous image reconstruction significantly. Going from one projection to three projections, the spatial resolution quantified by the full width at half maximum of the point-spread function (PSF) is improved from 2.6 pixels to 1.4 pixels (4 mm nominal resolution per pixel). Considering the shape of the PSF, the effective spatial resolution is improved from 16.9 pixels to 4.7 pixels. *In vivo* fMRI experiments using a two-choice reaction time tasks shows visual and sensorimotor cortical activity spatially consistent with typical EPI data, yet mInI offers 100 ms temporal resolution with the whole brain coverage. The mInI data with three projections revealed that the sensorimotor cortex was activated 700 ms after the visual cortex. mInI can be applied to BOLD-contrast fMRI experiments to characterize the dynamics of the activated brain areas with a high spatiotemporal resolution.

Keywords

event-related; fMRI; InI; visual; motor; MRI; inverse problem; projection

Correspondence: Fa-Hsuan Lin, Ph.D., Institute of Biomedical Engineering, National Taiwan University, 1, Sec. 4, Roosevelt Road, Taipei, Taiwan, fhlin@ntu.edu.tw, Tel: +886-2-33665264, Fax: +886-2-33669702.

Introduction

Functional magnetic resonance imaging (fMRI) (Belliveau et al., 1991) using blood-oxygen-level-dependent (BOLD) contrast (Kwong et al., 1992; Ogawa et al., 1990) has become a prevailing method of studying human brain function non-invasively. With a typical in-plane spatial resolution of 3–5 mm, acquisition of BOLD-contrast fMRI is usually accomplished by echo-planar imaging (EPI) (Mansfield, 1977) using fast gradient switching in order to complete 2D k-space traversal in approximately 80 ms per slice or 2 s with the whole brain coverage. The quest for a higher temporal resolution in fMRI has been motivated by, for example, its potential to monitor and to suppress physiological fluctuations not related to the hemodynamics in order to improve the sensitivity of detecting brain activity (Kruger and Glover, 2001; Lin et al., 2011). This is due to the fact that the conventional 0.5 Hz/volume sampling rate is too low to resolve the aliased cardiac (1.0–1.3 Hz) and respiratory (0.2 – 0.3 Hz) cycles. The other motivation for high temporal resolution fMRI is to provide hemodynamic timing information at neuronally relevant scale (Lin et al., 2010a). Additionally, it has been suggested that an fMRI with a faster sampling rate can significantly improve the power of detecting causal modulations among brain areas during tasks and cognition (Deshpande et al.; Kayser et al., 2009; Roebroeck et al., 2005).

With advances in radio-frequency (RF) receiver coil technology, the feasibility of accelerating MRI data acquisition rate via simultaneous data acquisition from multiple channels of an RF coil array and the associated image reconstruction algorithms in either image-space or k-space (Pruessmann et al., 1999; Sodickson and Manning, 1997) has been successfully demonstrated. MR inverse imaging (InI) is an extreme variant of such a parallel MRI strategy: using highly parallel detection, dynamic images with the associated statistical maps can be obtained at the 20 ms temporal resolution using minimal gradient encoding for 2D single slice imaging (Lin et al., 2006b). InI is closely related to the MR-encephalography (MREG) method (Hennig et al., 2007) and it has been applied to volumetric imaging with different reconstruction alternatives (Lin et al., 2010b; Lin et al., 2008a; Lin et al., 2008b; Liou et al., 2011). Currently, BOLD-contrast fMRI using InI can achieve 100 ms temporal resolution with whole-brain coverage and approximately 5 mm spatial resolution at cortex (Lin et al., 2010b; Lin et al., 2008a; Lin et al., 2008b).

InI and more generally pMRI reconstruct images by solving a system of linear equations. In contrast to solving over-determined inverse problems in typical pMRI applications, the InI image reconstruction has been intrinsically under-determined since the time-consuming partition encoding steps have been left out in order to achieve the temporal acceleration. The absence of gradient encoded spatial information along the partition encoding direction is complemented by RF coil sensitivity information and prior constraints. Consequently, InI has anisotropic spatial resolution. This challenge can be partially mitigated by optimizing k-space trajectory (Grotz et al., 2009). However, InI generally has a lower spatial resolution at the center of head and a higher spatial resolution at locations close to the RF coils.

In InI acquisitions, leaving out all partition encoding steps is equivalent to acquiring a projection image. In most BOLD-contrast fMRI experiments, repetitive measurements are usually required to compensate the relatively low contrast-to-noise ratio (CNR) in order to detect activated brain areas with a sufficient statistical significance. Such a data acquisition protocol opens up the possibility of combining InI acquisitions across different runs to improve the spatial resolution. Here we propose the multi-projection InI reconstruction method (mInI) to achieve fast 3D MR inverse imaging with an improved spatial resolution. Specifically, rather than repetitively measuring *the same projection images*, more spatial information can be obtained by changing the axes of frequency, phase, and partition encoding such that *different projection images* are acquired. The collection of projection

images can be combined to improve the spatial resolution in dynamic InI reconstructions. Compared to InI using only one projection image, as demonstrated in our numerical analysis, the mInI's encoding matrix is likely to be better conditioned because more measurements with distinct spatial information are included. This is due to the fact that different projection images from a coil array with evenly distributed coil elements in 3D can include non-redundant spatial information to thus to improve the conditioning of the mInI encoding matrix. As the COBRA method demonstrated the utility of a multi-projection acquisition strategy in 2D fMRI using an eight-channel coil array (Grotz et al., 2009), here we use numerical simulations and *in vivo* visuomotor fMRI data with a 32-channel head coil array to demonstrate that mInI's spatial resolution can be improved significantly compared to InI with only one single projection in 3D volumetric acquisition with whole brain coverage.

Material and methods

Participants and tasks

Written informed consents were obtained from participants ($n = 12$), in accord with the National Taiwan University Hospital and National Yang Ming University ethical committees. The participants were presented with left or right visual hemifield reversing (8 Hz) checkerboard stimuli in a rapid event-related fMRI design. The hemifield checkerboard subtended 4.3° visual angle and was generated from 24 evenly distributed radial wedges and eight concentric rings of equal radii. The stimuli were presented using Psychtoolbox (Brainard, 1997; Pelli, 1997). Stimulus duration was 500 ms; onset of each presentation was randomized with a uniform distribution to generate inter-stimulus intervals (ISIs) varying between 3 and 16 seconds. The visual stimuli were presented randomly at either left (L) or right (R) side of the screen. The participants were instructed to press the button with the ipsilateral hand to the visual stimulus as soon as possible. Thus the experiment included two conditions: right visual hemifield – right hand (R) and left visual hemifield – left hand (L) conditions. Twenty-four stimuli for each condition were presented during four 240 s runs, resulting in a total of 96 stimuli per participant.

Pulse sequence and data acquisition

Data were acquired with a 3T scanner (Tim Trio, Siemens, Erlangen, Germany) using a 32-channel head coil array. The pulse sequence for mInI is based on a blipped EPI sequence with whole brain volume excitation. InI acquisition consists of a reference scan, where all partition encoding steps are acquired, and multiple runs of accelerated scans, where partition encoding steps are left out in order to achieve a fast scanning rate. Previously reported InI studies (Lin et al., 2010b; Lin et al., 2008a; Lin et al., 2008b; Liou et al., 2011) used the EPI read-out along the z-axis (superior-inferior direction) and the phase encoding and partition encoding along the x-axis (left-right direction) and y-axis (anterior-posterior direction), respectively. Collecting only data with $k_y = 0$, this acquisition strategy leads to a time series of coronal slice projection images in the accelerated scan.

Different from InI where the partition, phase, and frequency encoding axes are kept the same for the whole experiment, mInI acquires data with different partition, phase, and frequency encoding axes across runs. Specifically, we acquired coronal projection images (partition, phase, and frequency encoding steps along y-, x-, and z-axis respectively), sagittal projection images (partition, phase, and frequency encoding steps along x-, z-, and y-axis respectively), and transverse projection images (partition, phase, and frequency-encoding steps along z-, y-, and x-axis respectively) in consecutive runs. Figure 1 illustrates the acquisition strategy. Reference scans with full partition encoding steps were acquired for each run separately. The imaging parameters were: FOV 256 mm × 256 mm × 256 mm; 64

× 64 × 64 image matrix, flip angle 30°, TR=100 ms, TE=30 ms, bandwidth=2520 Hz/pixel. The total acquisition time for the reference scan with two repetitions and 64 partitions was 12.8 s. For the functional scans, we used the same volume prescription, TR, TE, flip angle, and bandwidth as the reference scan. The principal difference was that the partition phase encoding was removed so that the full volume was excited, and the magnetizations were spatially encoded by a single-slice EPI trajectory, resulting in a projection image for each receiver coil. We collected four runs of functional scans with coronal projection images (partition encoding along anterior-posterior direction), four runs of functional scans with sagittal projection images (partition encoding along left-right direction), and four runs of functional scan with transverse projection images (partition encoding along superior-inferior direction). In each run, we collected 2,400 functional measurements after 60 dummy measurements to allow the steady state of the longitudinal magnetization to be reached. A total of twelve runs of data were acquired from each participant.

For comparison, typical multi-slice EPIs were also acquired with TR = 2 s, TE = 30 ms, flip angle = 90°, bandwidth = 2442 Hz/pixel, FOV = 220 by 220 by 120 mm, and an image matrix = 64 × 64 × 30. Four runs of EPI data were collected. Each run lasted for 4 minutes.

Structural T1-weighted MRIs of each participant were also acquired using a MPRAGE sequence (TR/TE/TI = 2,530/3.03/1100 ms, flip angle = 7°, partition thickness = 1.0 mm, image matrix = 256×224, 192 partitions, field-of-view = 25.6 cm × 22.4 cm).

Image reconstruction

Anatomical images were reconstructed using the FreeSurfer package (http://surfer.nmr.mgh.harvard.edu). The location of the gray-white matter boundary for each participant was estimated with an automatic segmentation algorithm to yield a triangulated mesh model with approximately 340,000 vertices (Fischl et al., 2001; Fischl et al., 1999a; Fischl et al., 1999b). This cortical model was then used to facilitate mapping of the structural image from native anatomical space to a standard cortical surface space (Dale et al., 1999; Fischl et al., 1999b). Across-subjects averaging was done by morphing individual data through a surface-based spherical coordinate system (Fischl et al., 1999a).

The mInI reconstruction started from processing the data in the time domain in order to derive the coefficients of the hemodynamic response basis function in each voxel of the projection image from each channel of the coil array. Specifically, we used Finite-Impulse-Response (FIR) basis functions (Burock and Dale, 2000) and General Linear Model (GLM) to allow a high degree of freedom in characterizing hemodynamic responses. The FIR basis was used to model a hemodynamic response of 30 s duration in time steps of 0.1 s with 6 s of pre-stimulus baseline. The design matrix of the GLM included modeled hemodynamic responses as the convolution between the visual stimulus onset and the FIR bases. Confounds of run-specific DC bias, linear drift, seven sine/cosine oscillations with frequencies of 1/480 Hz to 7/480 Hz (with 1/480 Hz step), and 32 grand averages of all projection image voxels for each RF channel were also included. The physiological noise originating from spontaneous cardiac and respiratory cycles has been shown to be a significant noise source at high field fMRI (Kruger and Glover, 2001). Thus synchronized physiological time series (cardiac pulses, respiratory cycles, and pulse and pulse oxymetry) were also included as regressos in the design matrix in order to account for the measurements fluctuations due to physiological noise. The coefficients of the hemodynamic response functions for each run and each channel of the RF coil array were calculated by the standard least square estimation. In summary, for each RF coil and every pixel in the coronal, sagittal, and transverse projection images, we obtained separate GLM-based FIR basis coefficients that were used in the following volumetric image reconstruction. GLM

FIR bases estimates during the baseline ($t<0$) were used to calculate the noise covariance matrix $\mathbf{C}$ between channels of the RF coil array.

The volumetric distribution of the hemodynamic response coefficients $\mathbf{x}(t)$ at time point t is related to the accelerated mInI acquisitions by a linear equation. Without loss of generality, we consider the coronal projection acquisitions first:

$$\mathbf{y}_0{}^{COR}(t)=\mathbf{A}_0{}^{COR}\mathbf{x}(t)+\varepsilon_0{}^{COR}(t), \quad [1]$$

where $\mathbf{y}_0{}^{COR}(t)$ is the collection of the estimated hemodynamic response function coefficients from all channels of the RF coil array using the coronal projection data. The matrix $\mathbf{A}_0{}^{COR}$ denotes a forward operator mapping the hemodynamic response coefficients in 3D onto coronal projection images. The operator $\mathbf{A}_0{}^{COR}$ is constructed from the empirically measured reference scan (partition encoding in the anterior-posterior direction) and it effectively integrates over all image voxels along the partition encoding (y-axis) direction. $\varepsilon_0{}^{COR}(t)$ is a vector of Gaussian noises. Performing the noise whitening, Eq. [1] becomes:

$$\begin{gathered}\mathbf{C}^{-1/2}=\Lambda^{1/2}\mathbf{U}^{H}\\ \mathbf{y}^{COR}(t)=\mathbf{A}^{COR}\mathbf{x}(t)+\varepsilon^{COR}(t),\\ \mathbf{y}^{COR}(t)=\mathbf{C}^{-1/2}\mathbf{y}_0{}^{COR}(t)\\ \mathbf{A}^{COR}=\mathbf{C}^{-1/2}\mathbf{A}_0{}^{COR}\\ \varepsilon^{COR}(t)=\mathbf{C}^{-1/2}\varepsilon_0{}^{COR}(t),\end{gathered} \quad [2]$$

where noise covariance matrix has been decomposed by the singular value decomposition: $\mathbf{C}=\mathbf{U}\,\Lambda\mathbf{U}^{H}$ with the superscript H denoting transpose and complex conjugation.

The mInI approach combines estimated hemodynamic response function coefficients from coronal, sagittal, and transverse projections. Thus Eq. [2] becomes:

$$\mathbf{y}(t)=\begin{bmatrix}\mathbf{y}^{COR}(t)\\ \mathbf{y}^{SAG}(t)\\ \mathbf{y}^{TRA}(t)\end{bmatrix}=\begin{bmatrix}\mathbf{A}^{COR}\\ \mathbf{A}^{SAG}\\ \mathbf{A}^{TRA}\end{bmatrix}\mathbf{x}(t)+\begin{bmatrix}\boldsymbol{\varepsilon}^{COR}(t)\\ \boldsymbol{\varepsilon}^{SAG}(t)\\ \boldsymbol{\varepsilon}^{TRA}(t)\end{bmatrix}=\mathbf{A}\mathbf{x}(t)+\boldsymbol{\varepsilon}(t), \quad [3]$$

where $\mathbf{y}(t)$ and $\boldsymbol{\varepsilon}(t)$ denote the vertical concatenation of hemodynamic response basis coefficients and noises for the same instant t from different projections. The matrix $\mathbf{A}$ denotes the vertical concatenation of the forward operators from different projections. The superscripts COR, SAG, and TRA represent coronal, sagittal, and transverse projections, respectively.

Eq. [3] differs from Eq. [2] in that the number of equations constraining the unknowns is increased threefold. Practically, using a 32-channel head coil array with image matrix of 64 × 64 × 64, the forward operator $\mathbf{A}$ for mInI using three projections consists of 64 × 64 × (3 × 32) rows and 64 × 64 × 64 columns. Depending on the number of projections concatenated in the forward operator $\mathbf{A}$ and the geometry of the coil array, the conditioning of $\mathbf{A}$ can be improved.

When $\mathbf{A}$ has sufficiently more non-redundant rows than columns, using a constraint of minimizing the ℓ^2-norm of $\boldsymbol{\varepsilon}(t)$ can solve Eq. [3] analytically:

$$\widehat{\mathbf{x}}(t)=\left(\mathbf{A}^{H}\mathbf{A}\right)^{-1}\mathbf{A}^{H}\mathbf{y}(t). \quad [4]$$

However, the matrix ($\mathbf{A}^H\mathbf{A}$) is too large (262,144-by-262,144) to be calculated and inverted explicitly. We thus use the conjugated gradients squared algorithm (CGS) (Sonneveld, 1989) to solve Eq. [3] iteratively.

To facilitate statistical inference from the mInI time series reconstruction results, the noise levels σ in the reconstructed images $\hat{\mathbf{x}}(t)$ were estimated from the standard deviation of the baseline data ($t < 0$). This approach was previously introduced in InI reconstruction (Lin et al., 2006a; Lin et al., 2010b; Lin et al., 2008a; Lin et al., 2008b; Liou et al.) and MEG/EEG source localization (Dale et al., 2000). Dynamic statistical parametric maps $\mathbf{s}(t)$ can be derived as the time-point by time-point ratio between the mInI reconstruction values $\hat{\mathbf{x}}(t)$ and the baseline noise estimates σ:

$$s(t)=\widehat{x}(t)/\sigma, \quad [5]$$

Performance measures—By calculating the condition number of the forward operator **A**, we can characterize the numerical tractability of the image reconstruction problem when different projections were jointly used. By definition, the condition number is the ratio between the largest and the smallest of the singular values of **A**. The condition numbers of the encoding matrices using one or two projections were calculated using a 32-channel array and an image matrix of 64 × 64 × 64. However, limited by available computer memory, we have to reduce image matrix to 32 × 32 × 32 as we calculated the condition number of the matrix **A** using three projections.

In order to avoid overly optimistic results in simulations when exactly the same forward operator is used in the genesis of synthetic data and inverse solutions (Somersalo and Kaipio, 2007), we used different forward operators from two measurements of three fully partition encoded reference scans. One reference scan was used to create the synthetic measurements in the simulation, and the other reference scan was used as the forward operator to reconstruct images, spatial resolution analysis based on point-spread function, and detection power using receiver-operating characteristic analysis (see below).

We studied the convergence of mInI reconstruction using the CGS algorithm by measuring the residual data fit error $\xi(k)=\sum_t \|y(t) - \mathbf{A}x^k(t)\|_2^2$ over iterations indexed by k. The normalized residual data fit error $\xi_n(k)$ was defined as

$$\xi_n(k)=\xi(k)/\xi(1). \quad [5]$$

This metric was chosen as the figure of merit because all quantities can be measured or calculated directly. The error $\xi(k)$ was calculated at each step over 200 iterations.

To evaluate the quality of reconstructing a static mInI image, we used three fully partition encoded reference scans to generate the forward operator **A**. Simulated mInI acquisition **y** was obtained from different reference scans without partition encoding. Ideally, the reconstructed volumetric image **x** should be a volume of 1, which corresponds to a static reference scan. For visualization, we averaged the sum-of-squares of three reference scans to generate a volume **r** and calculated the product between **x** and **r**. This product thus keeps features of the image. The mInI reconstruction error ρ was defined as

$$\rho = \frac{\sum |\mathbf{r}(\mathbf{1} - \mathbf{x})|}{\sum |\mathbf{r}|}, \quad [6]$$

where **1** represents a vector of 1. A smaller ρ reflects a more accurate reconstruction of the reference scan from the accelerated projection data.

The evaluation above is one way to check time-invariant reconstruction. Since mInI ultimately aims to be used in fMRI scan, it is desired to test if the sensitivity and specificity of detecting dynamic changes (e.g., localized brain activations in tasks) is improved when more projection data are used. Thus, we also performed an analysis based on of the receiver operating characteristic (ROC) curve (Creelman, 1998) to evaluate the mInI's power of detecting localized signal changes, similar to the BOLD contrast, using one, two, and three projections. Specifically, a volume of Gaussian random noise of the standard deviation of 0.28 was first created. Three clusters of voxels (3 × 3 × 3 voxels per cluster; two at the periphery and one at the center; 4 mm × 4 mm × 4 mm nominal resolution per voxel) were chosen as the sites of simulated BOLD activation. The magnitude of these three "activated" voxel clusters were adjusted to meet the simulation SNR, which was calculated as the average signal strength at three clusters of voxels over the standard deviation of the background Gaussian noise. SNRs were varied between 3.5, 4, 4.5, 5, 10, 15, 20, 25, 30, 35, 40, 45, and 50. To obtain average performance without being biased toward any realization of the noise, each simulation with a specified SNR was repeated 30 times. Given the sites of signal voxels, we calculated the true-positive rate and false-positive rate of detection for a predetermined threshold. As the threshold was then varied, we derived the ROC curve and used the area under the ROC curve (AUC) to quantify the detection power. The AUC value falls between 0.5 and 1 indicating the smallest and the largest detecting power, respectively.

The spatial resolution of mInI reconstruction was analyzed by the point spread function (PSF), which was numerically calculated by 1) creating an discrete impulse input image at one selected location, 2) simulating the ideal measurements across channels of the RF coil array and image indices in the project images (Eq, [3]), and 3) calculating the estimates $\hat{\mathbf{x}}$ using the CGS algorithm (Eq. [4]). This procedure was repeated at different location inside the FOV. We considered two ways of characterizing the spatial resolution based on the PSF. First, we used the full width at half maximum (FWHM) (Engel et al., 1997) of the PSF to quantify the spatial resolution. PSF was defined as the profile of the reconstructed $\hat{\mathbf{x}}$ and we measured the FWHM of the profile (Eq. [4]). We parametrically studied the reconstruction using one projection (coronal projection), two projections (coronal + sagittal projections), and three projections (coronal + sagittal + transverse projections) at two locations: one was around the center of the FOV and the other one was at the periphery of the FOV. Second, in order to take the intensity distribution of the PSF into account (Buxton, 2002), we also evaluate the *effective resolution* of the i^{th} image voxel by

$$\overline{PSF(i)} = \int PSF(x)dx / PSF(i), \quad [7]$$

where *PSF(x)* denotes the value of the PSF at the x^{th} voxel and *PSF(i)* denotes the value of the PSF at the i^{th} voxel, where a discrete impulse input image was created.

Results

Conditioning of forward operator

We first studied how the condition number changes when different projection images were included in the forward operator. The condition numbers of the forward operator with using

one (coronal) or two (coronal + sagittal) projections in 64 × 64 × 64 image matrix were 8.16×10^{23} and 7.19×10^{15} respectively. The condition numbers of the forward with using one (coronal), two (coronal + sagittal), and three (coronal + sagittal +transverse) projections in 32 × 32 × 32 image matrix were 9.18×10^{12}, 2.76×10^{7}, and 1.23×10^{7} respectively. These numbers clearly indicated the improvement of the conditioning as the number of projection images increased. Note that the largest change was from using one coronal projection to using two (coronal and sagittal) projections.

Simulations

We studied the convergence properties of the CGS image reconstruction algorithm numerically. Figure 2 shows the normalized residual data fit error ξ over 200 iterations. We observed a monotonic and sharp decrease of ξ from 1 to 0.01 in the first 10 iterations. After 200 iterations, ξ was reduced to less than 0.01. This convergence behavior was found to be similar among reconstructions using one projection (coronal projection), two projections (coronal + sagittal projections), and three projections (coronal + sagittal + transverse projections). Based upon the results of the convergence analysis, 20 CGS iterations were considered sufficient for stable image reconstruction and this value was used for the remainder of this study.

Figure 3 shows the mid-coronal, mid-sagittal, and mid-transverse slices of the reconstructed volumes using one (coronal), two (coronal + sagittal), and three (coronal + sagittal + transverse) projections. We also report the associated reconstruction error ρ. Prominent bi-hemispheric artifacts of signal loss were found in temporal lobe in the mid-transverse slice when using only coronal projection data. The mid-sagittal slice showed signal loss in the cerebellum and orbitofrontal lobe. The mid-coronal slice had significant signal loss in the brain stem. These artifacts were potentially due to strong localized off-resonance, which contributed to fast phase changes across image voxels and consequently signal loss in the projection image. Since the minimum-norm estimates favors reconstructions with minimal power, the loss of signal in the projection image leads to lower intensity in the reconstruction. These types of artifact were significant improved when two (coronal + sagittal) projections were used. In particular, the susceptibility ‘holes’ in one coronal projection InI reconstruction were filled in by the combination with a second sagittal projection data (Figure 3). Note that although the coronal and sagittal projection data had the same read-out direction along the z-axis (superior/inferior direction), the phase encoding axes were different: the coronal projection data had the phase encoding direction along the left/right direction and sagittal data along the anterior/posterior direction. Figure 3 suggested that combining 2-projection data with inconsistent phase encoding axes can actually reduce the susceptibility artifact. Numerically, the reconstruction error ρ defined in Eq. 6 reduced from 0.47 to 0.38. Marginal image improvement was found between mInI using 2 projections and mInI using 3 projections mInI. This is likely due to the limited spatial information augmented from the additional transverse projection images in 3-projection mInI. Using three projections, the reconstruction error was further improved by showing an even smaller ρ. Such a marginal improvement of the construction is consistent with the calculation on the conditioning number of the encoding matrix above and the spatial resolution analysis below.

The detection power of mInI to local signal changes as the BOLD contrast was studied by evaluating the AUC in the simulation across different SNRs. Figure 4 shows the AUC using one (coronal), two (coronal + sagittal), and three (coronal + sagittal + transverse) projections over the SNR from 3.5 to 50. We observed a progressive increase of the AUC as the SNR increased. Comparing between mInI using one, two, or three projections at the same SNR, the AUC is always larger when more projections were used. This difference is more prominent as SNR is lower than 20. For example, at SNR = 10, AUC increased from 0.9921

to 0.9994 and 0.9995 when one, two, and three projections were used for reconstruction respectively. One mid-transverse slice of the simulation is also shown in Figure 4 for SNR = 5, 15, and 50. We found that InI reconstructions with more projections can suppress the blurring and improve the accuracy of detecting localized signal changes from noisy data.

Figure 5 shows the spatial analysis by evaluating the FWHM of the PSF for an image voxel at the periphery of the FOV. Note that the partition encoding direction in this simulation is along the left-right direction. The peak of the PSFs using one, two, and three projections was found with no bias. However, strong ripples were found in InI reconstruction using only one coronal projection images. The PSF was found much smoother when two projections (coronal + sagittal) were used. The reconstruction using three projections had a similar PSF to that of the two projections reconstruction with an even narrower width (quantified by the FWHM of the PSF). Note that the PSF is rather unsmooth and anisotropic. Thus using full-width-half-maximum for PSF quantification can only provide partial information about the spatial resolution. Quantitatively, the FWHM of the PSF decreased from 1.2, 1.1, and 1.0 pixel using one, two, and three projections respectively. The effective resolution decreased from 7.5, 3.1, and 1.6 pixel using one, two, and three projections respectively.

For image voxel at the center of the FOV, we found that the FWHM of the PSF was larger and the shape was less smooth than the PSF of an image voxel at the periphery of the FOV (Figure 5B). Again, the FWHM monotonically decreased as the number of projections increased. The FWHM for reconstruction using one, two, three projections was 2.6, 1.6, and 1.3 pixels respectively. The effective resolutions were 13.6, 6.7, and 5.0 pixels respectively. Taken together, mInI can improve the spatial resolution quantified by FWHM by approximately 29% and 39% by using two and three orthogonal projections respectively. The effective resolution can be improved respectively by approximately 53% and 69% when two and three projections are used in mInI reconstruction.

Table 1 shows the average and the standard deviation of the FWHM and the effective resolution of the mInI reconstructions using one, two, and three projections. We observed that regardless of the metrics, the spatial resolution monotonically increased when more projections were used.

Figure 6 shows the effective resolution at mid-coronal, mid-sagittal, and mid-transverse slice of the image volume. More projections used in mInI reconstruction can provide more uniform and higher effective resolution along different slice direction. The effective resolution is lower at the center of the FOV than at the periphery of the FOV, consistent with the results in Figure 5.

In vivo experiments

The spatial distributions of the activated brain areas in a visuomotor task at four seconds after the onset of the visual stimuli using 3 projections mInI and EPI are shown in Figure 7. It should be noted that 3 projections mInI used 50% and 200% more data (and thus the acquisition time accordingly) than 2 projections mInI and 1 projection InI respectively. However, all data show strong activation in the visual cortex and sensorimotor cortices n the medial and lateral aspect of the inflated brain cortex. The spatial distributions of these functional areas were visually similar between mInI and EPI. Quantitatively, the shift of the center of mass between EPI and mInI in the sensorimotor was 0.96, 0.93, and 0.33 mm using one, two, and three projections, respectively. Additionally, activity in supplementary motor area and higher order visual areas in the ventral and dorsal streams were found in both EPI and mInI. The spatial patterns of activity were not exactly identical, potentially due to intra-subject and inter-scan variability (Jensen and Kapur, 2003; Leontiev and Buxton, 2007).

The time courses of the hemodynamic responses in the visual and sensorimotor cortex based on mInI using three projections are shown in Figure 8. Based on the high temporal resolution mInI measurements, we found that the hemodynamic response in the visual cortex preceded that in the sensorimotor cortex. To quantify the timing, the hemodynamic responses with 0.1 s resolution were fitted by a model consisting of two exponentials (Glover, 1999). Based on the model, three timing indices were obtained: Onset, time-to-half (TTH), and time-to-peak (TTP). The Onset is defined as the instant when a straight line fitted between 10% and 90% of the rising edge of the hemodynamic response function intersects the time axis. The TTH and TTP are the instants when the response reaches 50% and 100% of the peak value, respectively. The visual cortex has Onset, TTH, and TTP of 1.09 s, 2.40 s, and 4.60 s respectively using three projections. The sensorimotor cortex has Onset, TTH, and TTP of 1.87 s, 3.10 s and 5.00 s respectively using three projections. The hemodynamic response in the visual cortex preceded that in the sensorimotor cortex by 0.78 s, 0.7 s, and 0.4 s in Onset, TTH, and TTP using three projections. While using different amount of data may affect the significance level of activated brain areas, the interregional hemodynamic timing (Figure 8) was based on amplitude-normalized hemodynamic responses. Thus, this result likely remains the same when the amount of mInI data is adjusted to be comparable to that of the 1-projection InI data, since the amount of data most likely affects the residual variance of the estimated hemodynamic response function (HRF) and accordingly scales the dynamic statistics of the estimated HRF. Such a scaling has no effect on the estimated timing indices of the hemodynamic responses.

Discussion

In this study we demonstrated both theoretically and empirically that spatial resolution of fast (10 Hz) whole-head fMRI can be substantially improved by integrating spatial information from multiple projections. Compared to InI using only one projection, three-projection mInI can improve the spatial resolution quantified by the FWHM of PSF in the cortex by 17% (1.2 pixels to 1.0 pixels). At the deep brain area, the FWHM of PSF was found improved by 50% (2.6 pixels to 1.3 pixels). Since fMRI typically requires multiple runs to obtain sufficient contrast-to-noise ratio to detect activated brain areas, mInI acquisitions can be easily implemented empirically by collecting different projections in different runs. Note that these results were calculated from empirical fully gradient encoded data, thus the susceptibility artifacts along different phase encoding directions were included already.

mInI achieves fast BOLD-contrast fMRI using multiple projections. This strategy has been previously proposed by the COBRA (Grotz et al., 2009) to combine different projections to achieve high temporal resolution (TR = 80 ms) 2D BOLD-contrast fMRI using an eight-channel coil array. Our mInI demonstrates the technical feasibility and spatiotemporal resolution of 3D BOLD-contrast fast fMRI using a 32-channel coil array. More importantly, projections in the CORBA had a common axis. mInI is a further generalization of COBRA allowing projections over 3D. This is especially well suited to the 32-channel coil array based on a soccer-ball geometry (Wiggins et al., 2009; Wiggins et al., 2006), where spatial information is more evenly distributed over the whole head.

Practically, mInI reconstruction can be computationally intensive. The encoding matrix in our study had $64 \times 64 \times 32 \times 3$ rows and $64 \times 64 \times 64$ columns using three projections. Using 8-byte floats and complex numbers, the encoding matrix takes about 1.5 GBytes memory space. At present, direct inversion on such a matrix is computationally intractable. We thus proposed the iterative CGS solver for image reconstruction (Eq. 4).

Although mathematically the encoding matrix in mInI (Eq. 3) in our protocol (3 projections; 32-channel head array, 64 × 64 × 64 image matrix) has more columns than rows in mInI with three projections, we still did not have perfect reconstruction with PSF being a discrete delta function over the FOV (Figure 5). In fact, the conditioning number of the encoding matrix is still rather large (1.23×10^7). However, the conditioning number was greatly reduced from 1-projection InI (9.18×10^{12}) to 2-projection mInI (2.76×10^7). This suggests that while the encoding matrix still ill-conditioned, the uncertainty of the image reconstruction, which can be related to the spatial resolution of the reconstructed image, is indeed improved by combining more projection data. This was supported by point-spread function analyses (Figures 5 and 6).

Previously it has been suggested that the limit of acceleration along an encoding axis using RF coil sensitivity is between 3 and 4 fold acceleration under the constraint of the allowed noise amplification (g-factor ≈ 1) and isotropic reconstructed image voxels (Wiesinger et al., 2004). This is different from our study, which explored how much the reconstructed image voxels are blurred as more projection data are included. Both approaches can be regarded as studying how RF coil sensitivity and k-space trajectory can be optimally combined from two distinct perspectives: either reducing k-space acquisitions from a fully gradient encoded case to see the limit of the maximal acceleration with the allowed image quality penalty (Wiesinger et al., 2004), or increasing k-space acquisitions from a minimally gradient encoded case to understand how image resolution is improved.

One major concern of the mInI is that the data were acquired from three consecutive independent runs. The reference scans were also acquired separately. Such an acquisition protocol can make the reconstructed mInI prone to motion artifacts, which will degrade the consistency between the reference scan and the accelerated scans. Cautions must be taken, such as using appropriate fixation during data acquisition, in order to alleviate this potential problem.

The other potential source of deteriorating the consistency between the mInI reference scan and the accelerated scan is the physiological noise. fMRI physiological noise is signal dependent (Kruger and Glover, 2001) and can lead to pronounced amplitude variation in the projection images and therefore data inconsistency between the reference and accelerated scans. Such inconsistency will be eventually reflected in the increased noise variance in the general linear model analysis and the decreased power of detecting activated brain areas. One way of mitigating this challenge is to include the physiological signals (EKG, breathing, and pulse oxymetry) into the design matrix as confounding vectors as we did. Alternatively, it is possible to suppress physiological noises in the projection data before the general linear model analysis using other algorithm (Lin et al., 2011).

The trajectory of mInI is the central partition (no partition encoding) of the echo-volumar imaging. Other sophisticated trajectories aiming at a higher spatiotemporal resolution, such as single-shot Rosette trajectory (Zahneisen et al., 2011a), has been suggested. Recently, multiple concentric shell trajectory has also been realized to improve the spatial resolution of fast fMRI (Zahneisen et al., 2011b). However, the essential difference between mInI and these methods is that the mInI attempts to improve the conditioning of the encoding matrix, while Rosette and concentric shell trajectories still solve pretty under-determined inverse problem with necessary mathematical priors to complete image reconstructions.

We noticed that the spatial resolution of each projection in InI is quite different: The highest bandwidth is across partition encoding steps and thus blurring due to T2* decay and distortion due to susceptibility is negligible. Then frequency encoding direction has also rather high bandwidth (2520 Hz/pixel) to avoid spatial smoothing and distortion. The lowest

bandwidth is along the phase encoding direction. This study used a read-out bandwidth (2520 Hz/pixel) common to fMRI experiments. Furthermore, combining multiple projections can be regarded as smoothing distortion and spatial resolution across different projections. Accordingly, the spatial resolution of mInI is rather homogeneous (Figure 6).

The data presented here are mInI reconstructions using different projections acquired from different runs. Since the goal is to reveal time-locked hemodynamic responses with respect to the stimulus onset, with the assumption of stationary BOLD responses, taking measurements with different projections across runs is a straightforward way to collect mInI data in practice. However, such an acquisition method cannot be used to study dynamic changes of the BOLD responses, such as effects related to habituation, learning over the acquisition period, and resting state fluctuation. Specifically, acquiring mInI data with different projection images from different runs lost the possibility of detecting dynamic variations and variations between consecutive activation episodes. Reconstructing mInI data across runs using one reference scan acquired separately is also prone to artifacts from motional displacement between scans. Thus the reproducibility of the results can be suboptimal. However, it is possible to modify the pulse sequence such that the InI projection alternates the partition encoding direction dynamically to generate mInI data to study non-stationary features of fMRI, such as trial-by-trial variability. It should be noted that mInI using either identical or different encoding axes can develop steady state free precession (SSFP) signal as long as there is a train of RF pulses with TR < T2 (Zhao et al., 2000). B_0 fluctuations originating from respiration, physical movement outside the FOV, and system instability can cause SSFP temporal variation. It has been suggested that a strong crusher can be used to minimize these temporal noise fluctuations (Zhao et al., 2000). In fact, our experiment used a crusher gradient of 20 mT/m strength and 10 ms duration, as previously suggested (Zhao et al., 2000). However, since the suggested strong crusher was studied with TR = 200 ms, InI and mInI may require further increase the crusher moment to reduce the SSFP signal disturbance by increasing the crusher duration or strength.

mInI is technically less complicated than the echo-volume imaging (EVI) (Mansfield et al., 1994; Mansfield et al., 1995; Song et al., 1994), which also aims to achieve high spatial resolution imaging in hundreds of milliseconds. One concern of EVI is that the spatial resolution is rather inhomogeneous as the result of different bandwidths in three orthogonal directions. Particularly, the narrowest bandwidth in EVI is around 100 Hz/pixel (Witzel et al., 2011), thus the distortion and spatial resolution becomes rather poor in that specific direction. mInI mitigates this challenge by exploiting the requirement of repetitive measurements in BOLD fMRI experiments due to low contrast-to-noise ratio. By combining different projections over time, mInI integrates spatial information across acquisitions. However, applications that require single-shot acquisition cannot use mInI.

In conclusion, we demonstrated the feasibility of mInI to improve the spatial resolution of high temporal resolution (10 Hz/volume) BOLD-contrast fMRI with the whole-brain coverage. Such a temporal sampling rate is already about twenty times faster than that of conventional multi-slice EPI. This imaging acquisition technique can be used to study fine temporal features of hemodynamics, to monitor/suppress physiological noises, and in other dynamic MRI applications where fast acquisition is critical.

Acknowledgments

The authors thank Drs. Jonathan R. Polimeni and Joseph B. Mandeville technical supports and inspiring discussion. This work was supported by National Institutes of Health Grants by R01DA14178, R01HD040712, R01NS037462, P41RR14075, R01EB006847, R01EB000790, R01MH083744, National Center for Research Resources, NSC 98-2320-B-002-004-MY3, NSC 100-2325-B-002-046 (National Science Council, Taiwan), NHRI-EX100-9715EC

(National Health Research Institute, Taiwan), Academy of Finland (127624 and the FiDiPro program), Finnish Cultural Foundation, and Finnish Foundation for Technology Promotion.

References

Belliveau JW, Kennedy DN Jr, McKinstry RC, Buchbinder BR, Weisskoff RM, Cohen MS, Vevea JM, Brady TJ, Rosen BR. Functional mapping of the human visual cortex by magnetic resonance imaging. Science. 1991; 254:716–719. [PubMed: 1948051]

Brainard DH. The Psychophysics Toolbox. Spat Vis. 1997; 10:433–436. [PubMed: 9176952]

Burock M, Dale A. Estimation and detection of event-related fMRI signals with temporally correlated noise: a statistically efficient and unbiased approach. Hum Brain Mapp. 2000; 11:249–260. [PubMed: 11144754]

Buxton, RB. Introduction to functional magnetic resonance imaging: principles and techniques. Cambridge University Press; Cambridge, UK; New York: 2002.

Creelman CD. Signal detection theory and ROC analysis in psychology and diagnostics: Collected papers. Contemporary Psychology. 1998; 43:840–841.

Dale AM, Fischl B, Sereno MI. Cortical surface-based analysis. I. Segmentation and surface reconstruction. Neuroimage. 1999; 9:179–194. [PubMed: 9931268]

Dale AM, Liu AK, Fischl BR, Buckner RL, Belliveau JW, Lewine JD, Halgren E. Dynamic statistical parametric mapping: combining fMRI and MEG for high-resolution imaging of cortical activity. Neuron. 2000; 26:55–67. [PubMed: 10798392]

Deshpande G, Sathian K, Hu X. Effect of hemodynamic variability on Granger causality analysis of fMRI. Neuroimage. 52:884–896. [PubMed: 20004248]

Engel SA, Glover GH, Wandell BA. Retinotopic organization in human visual cortex and the spatial precision of functional MRI. Cerebral Cortex. 1997; 7:181–192. [PubMed: 9087826]

Fischl B, Liu A, Dale AM. Automated manifold surgery: constructing geometrically accurate and topologically correct models of the human cerebral cortex. IEEE Trans Med Imaging. 2001; 20:70–80. [PubMed: 11293693]

Fischl B, Sereno M, Tootell R, Dale A. High-resolution inter-subject averaging and a coordinate system for the cortical surface. Hum Brain Mapp. 1999a; 8:272–284. [PubMed: 10619420]

Fischl B, Sereno MI, Dale AM. Cortical surface-based analysis. II: Inflation, flattening, and a surface-based coordinate system. Neuroimage. 1999b; 9:195–207. [PubMed: 9931269]

Glover GH. Deconvolution of impulse response in event-related BOLD fMRI. Neuroimage. 1999; 9:416–429. [PubMed: 10191170]

Grotz T, Zahneisen B, Ella A, Zaitsev M, Hennig J. Fast Functional Brain Imaging Using Constrained Reconstruction Based on Regularization Using Arbitrary Projections. Magnetic Resonance in Medicine. 2009; 62:394–405. [PubMed: 19526512]

Hennig J, Zhong K, Speck O. MR-Encephalography: Fast multi-channel monitoring of brain physiology with magnetic resonance. Neuroimage. 2007; 34:212–219. [PubMed: 17071111]

Jensen J, Kapur S. Introduction to functional magnetic resonance imaging: Principles and techniques. Canadian Journal of Psychiatry-Revue Canadienne De Psychiatrie. 2003; 48:134–134.

Kayser AS, Sun FT, D'Esposito M. A comparison of Granger causality and coherency in fMRI-based analysis of the motor system. Hum Brain Mapp. 2009; 30:3475–3494. [PubMed: 19387980]

Kruger G, Glover GH. Physiological noise in oxygenation-sensitive magnetic resonance imaging. Magn Reson Med. 2001; 46:631–637. [PubMed: 11590638]

Kwong KK, Belliveau JW, Chesler DA, Goldberg IE, Weisskoff RM, Poncelet BP, Kennedy DN, Hoppel BE, Cohen MS, Turner R, Cheng H, Brady TJ, Rosen BR. Dynamic magnetic resonance imaging of human brain activity during primary sensory stimulation. Proc Natl Acad Sci U S A. 1992; 89:5675–5679. [PubMed: 1608978]

Leontiev O, Buxton RB. Reproducibility of BOLD, perfusion, and CMRO2 measurements with calibrated-BOLD fMRI. Neuroimage. 2007; 35:175–184. [PubMed: 17208013]

Lin, F-H.; Witzel, T.; Raij, T.; Ahveninen, J.; Belliveau, JW. Relative Timing of Brain Activations Revealed by Ultra-Fast MR Inverse Imaging (InI). Proc. Intl. Soc. Mag. Reson. Med; Stockholm, Sweden. 2010a. p. 268

Lin FH, Nummenmaa A, Witzel T, Polimeni JR, Zeffiro TA, Wang FN, Belliveau JW. Physiological noise reduction using volumetric functional magnetic resonance inverse imaging. Hum Brain Mapp. 2011

Lin FH, Wald LL, Ahlfors SP, Hamalainen MS, Kwong KK, Belliveau JW. Dynamic magnetic resonance inverse imaging of human brain function. Magn Reson Med. 2006a; 56:787–802. [PubMed: 16964616]

Lin FH, Wald LL, Ahlfors SP, Hamalainen MS, Kwong KK, Belliveau JW. Dynamic magnetic resonance inverse imaging of human brain function. Magnetic Resonance in Medicine. 2006b; 56:787–802. [PubMed: 16964616]

Lin FH, Witzel T, Chang WT, Wen-Kai Tsai K, Wang YH, Kuo WJ, Belliveau JW. K-space reconstruction of magnetic resonance inverse imaging (K-InI) of human visuomotor systems. Neuroimage. 2010b; 49:3086–3098. [PubMed: 19914383]

Lin FH, Witzel T, Mandeville JB, Polimeni JR, Zeffiro TA, Greve DN, Wiggins G, Wald LL, Belliveau JW. Event-related single-shot volumetric functional magnetic resonance inverse imaging of visual processing. Neuroimage. 2008a; 42:230–247. [PubMed: 18538587]

Lin FH, Witzel T, Zeffiro TA, Belliveau JW. Linear constraint minimum variance beamformer functional magnetic resonance inverse imaging. Neuroimage. 2008b; 43:297–311. [PubMed: 18672071]

Liou ST, Witzel T, Numenmaa A, Chang WT, Tsai KW, Kuo WJ, Chung HW, Lin FH. Functional magnetic resonance inverse imaging of human visuomotor systems using eigenspace linearly constrained minimum amplitude (eLCMA) beamformer. Neuroimage. 55:87–100. [PubMed: 21134470]

Liou ST, Witzel T, Numenmaa A, Chang WT, Tsai KW, Kuo WJ, Chung HW, Lin FH. Functional magnetic resonance inverse imaging of human visuomotor systems using eigenspace linearly constrained minimum amplitude (eLCMA) beamformer. Neuroimage. 2011; 55:87–100. [PubMed: 21134470]

Mansfield P. Multi-Planar Image-Formation Using Nmr Spin Echoes. Journal of Physics C-Solid State Physics. 1977; 10:L55–L58.

Mansfield P, Coxon R, Glover P. Echo-planar imaging of the brain at 3.0 T: first normal volunteer results. J Comput Assist Tomogr. 1994; 18:339–343. [PubMed: 8188896]

Mansfield P, Coxon R, Hykin J. Echo-volumar imaging (EVI) of the brain at 3.0 T: first normal volunteer and functional imaging results. J Comput Assist Tomogr. 1995; 19:847–852. [PubMed: 8537514]

Ogawa S, Lee TM, Kay AR, Tank DW. Brain magnetic resonance imaging with contrast dependent on blood oxygenation. Proc Natl Acad Sci U S A. 1990; 87:9868–9872. [PubMed: 2124706]

Pelli DG. The VideoToolbox software for visual psychophysics: transforming numbers into movies. Spat Vis. 1997; 10:437–442. [PubMed: 9176953]

Pruessmann KP, Weiger M, Scheidegger MB, Boesiger P. SENSE: Sensitivity encoding for fast MRI. Magnetic Resonance in Medicine. 1999; 42:952–962. [PubMed: 10542355]

Roebroeck A, Formisano E, Goebel R. Mapping directed influence over the brain using Granger causality and fMRI. Neuroimage. 2005; 25:230–242. [PubMed: 15734358]

Sodickson DK, Manning WJ. Simultaneous acquisition of spatial harmonics (SMASH): Fast imaging with radiofrequency coil arrays. Magnetic Resonance in Medicine. 1997; 38:591–603. [PubMed: 9324327]

Somersalo E, Kaipio J. Statistical inverse problems: Discretization, model reduction and inverse crimes. Journal of Computational and Applied Mathematics. 2007; 198:493–504.

Song AW, Wong EC, Hyde JS. Echo-volume imaging. Magn Reson Med. 1994; 32:668–671. [PubMed: 7808270]

Sonneveld P. Cgs, a Fast Lanczos-Type Solver for Nonsymmetric Linear-Systems. Siam Journal on Scientific and Statistical Computing. 1989; 10:36–52.

Wiesinger F, Boesiger P, Pruessmann KP. Electrodynamics and ultimate SNR in parallel MR imaging. Magn Reson Med. 2004; 52:376–390. [PubMed: 15282821]

Wiggins GC, Polimeni JR, Potthast A, Schmitt M, Alagappan V, Wald LL. 96-Channel receive-only head coil for 3 Tesla: design optimization and evaluation. Magn Reson Med. 2009; 62:754–762. [PubMed: 19623621]

Wiggins GC, Triantafyllou C, Potthast A, Reykowski A, Nittka M, Wald LL. 32-channel 3 Tesla receive-only phased-array head coil with soccer-ball element geometry. Magn Reson Med. 2006; 56:216–223. [PubMed: 16767762]

Witzel T, Polimeni JR, Lin FH, Numenmaa A, Wald LL. Single-Shot Whole Brain Echo Volume Imaging for Temporally Resolved Physiological Signals in fMRI. Proc Intl Soc Magn Reson Med. 2011:633.

Zahneisen B, Grotz T, Lee KJ, Ohlendorf S, Reisert M, Zaitsev M, Hennig J. Three-dimensional MR-encephalography: Fast volumetric brain imaging using rosette trajectories. Magn Reson Med. 2011a; 65:1260–1268. [PubMed: 21294154]

Zahneisen B, Grotz T, Zaitsev M, Hennig J. Ultra Fast Volumetric Functional Imaging using Single Shot Concentric Shells Trajectories. Proc Intl Soc Magn Reson Med. 2011b:4360.

Zhao X, Bodurka J, Jesmanowicz A, Li SJ. B(0)-fluctuation-induced temporal variation in EPI image series due to the disturbance of steady-state free precession. Magn Reson Med. 2000; 44:758–765. [PubMed: 11064411]

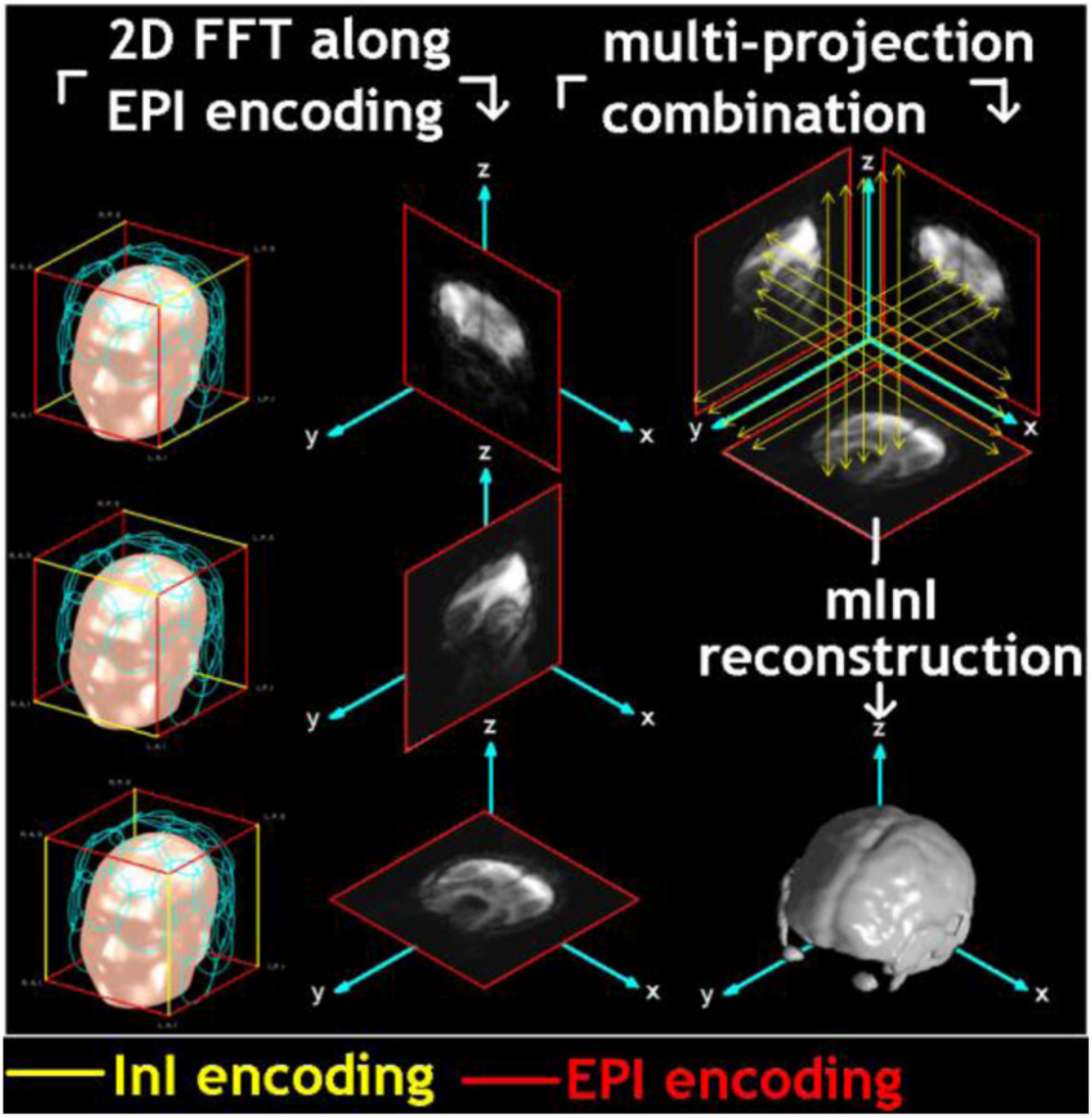

Figure 1.
The acquisition and reconstruction of mInI. The InI leaves out partition encoding steps. The acquired data are 2D projection images encoded by EPI phase and frequency encoding (red lines). The missed spatial information is derived by solving inverse problem (yellow lines). The mInI combines different projection images to include more spatial information to improve the conditioning of the mInI encoding matrix in the image reconstruction.

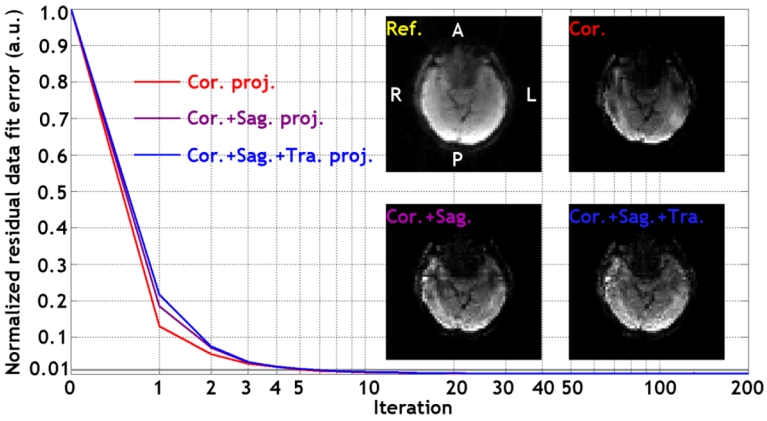

Figure 2.

The normalized residual data fit error $\xi_n(k)$ and the reconstructed images over CGS iterations. The plot shows the residual errors at different iterations using one (coronal), two (coronal + sagittal), and three (coronal + sagittal + transverse) projections. The reference image and the reconstructed mid transverse images at the 20^{th} iteration using one (coronal), two (coronal + sagittal), and three (coronal + sagittal + transverse) projections were shown in the figure inlet. A, P, R, and L denotes the anterior, posterior, right, and left.

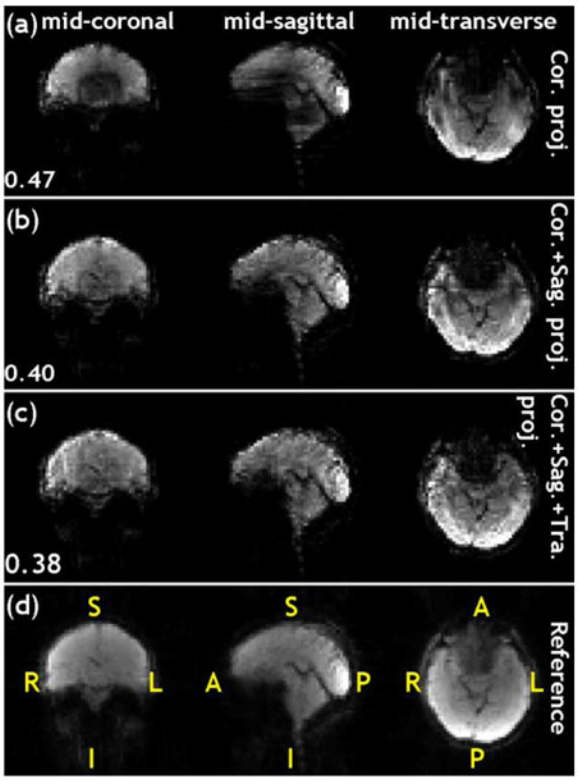

Figure 3.

Reference and reconstructed mInI images. The row A shows the reconstructed mInI images using only coronal projection; row B shows the reconstructed mInI images using coronal and sagittal projections; row C shows reconstructed mInI images using coronal, sagittal, and transverse projections; row D shows the reference images. R, L, A, P, S, and I denotes the right, left, anterior, posterior, superior, and inferior directions respectively. The number at left-down side of each reconstructed images represented the reconstruction error.

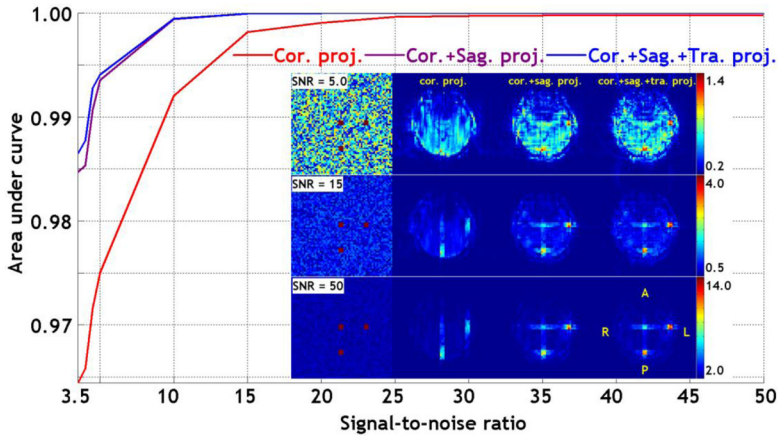

Figure 4.

The AUC at different SNRs using one (coronal), two (coronal + sagittal), and three (coronal + sagittal + transverse) projections. The image inside the figure shows the location of the simulated “signal” voxels and the reconstructed mid-transverse images at the SNR = 5, 15, 50 using one (coronal), two (coronal + sagittal), and three (coronal + sagittal + transverse) projections. A, P, R, and L denotes the anterior, posterior, right, and left.

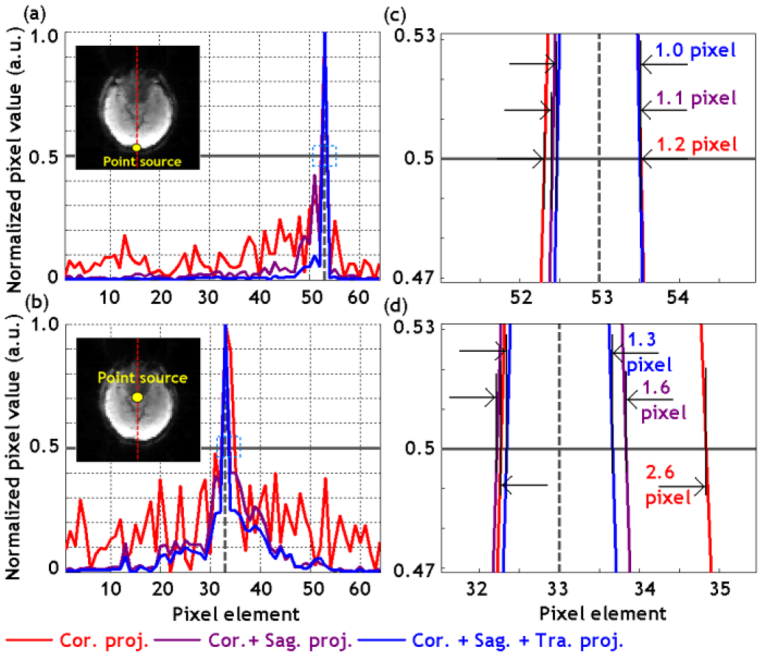

Figure 5.

A: the PSFs for a source voxel around the FOV periphery using coronal projection (red), coronal + sagittal projection (purple), and coronal + sagittal + transverse projections (blue). B: The PSFs for a source voxel around the FOV center using coronal projection (red), coronal + sagittal projection (purple), and coronal + sagittal + transverse projections (blue). The panels at right show the magnified portion of the PSFs around the 50% of the peak.

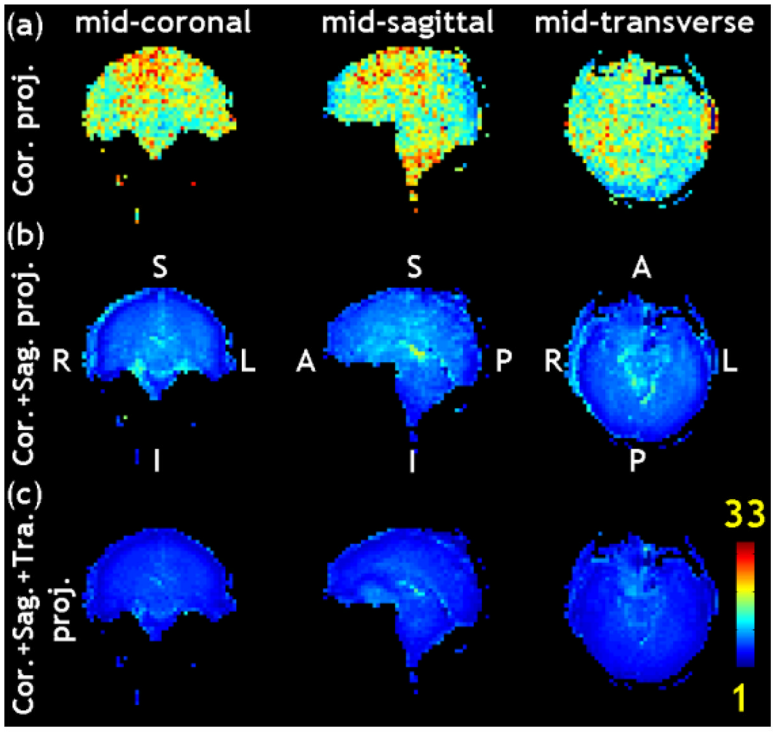

Figure 6.
The distribution of the effective resolution. The top row shows the effective resolution using only coronal projection; the middle row shows the effective resolution using coronal and sagittal projections; the bottom row shows effective resolution using coronal, sagittal, and transverse projections. R, L, A, P, S, and I denotes the right, left, anterior, posterior, superior, and inferior directions respectively.

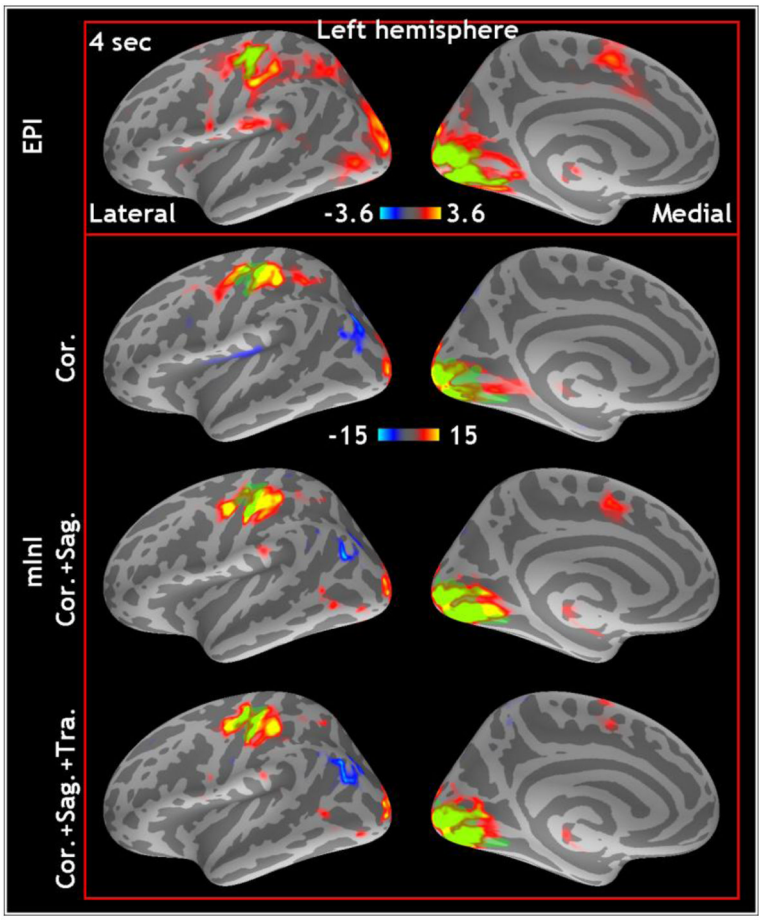

Figure 7.
Volumetric distribution of averaged activated areas at the 4 second after the onset of the visual stimulation and rendering on the inflated left hemisphere. The volumetric distributions are revealed by EPI and mInI reconstruction combining one (coronal), two (coronal + sagittal), and three (coronal + sagittal + transverse) projections.

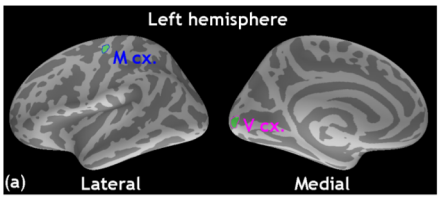

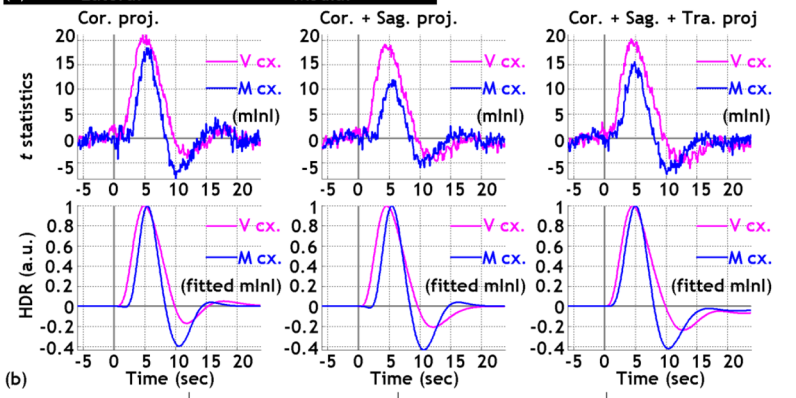

(c)

		Cor.	Cor. + Sag.	Cor. + Sag. + Tra.
Visual	Onset (s)	1.47	1.19	1.09
	TTH (s)	2.80	2.50	2.40
	TTP (s)	4.90	4.60	4.60
Sensorimotor	Onset (s)	2.72	2.67	1.87
	TTH (s)	3.80	3.80	3.10
	TTP (s)	5.40	5.14	5.00

Figure 8.

Averaged hemodynamic response on the functional visuomotor system. The dynamic *t*-statistics ranging from 6 s before to 23 s after the onset of the visual stimulation (0 s) are selected from the region of interesting of the visual (pink) and motor cortex (blue) of inflated left hemisphere and was shown at (a). (b) shows the *t*-statistics and fitted hemodynamic response for averaged of visual (pink) and sensorimotor (blue) cortex. The onset, TTH, and TTP of the fitted hemodynamic response for visual and sensorimotor cortex are shown at (c).

Table 1

The average and standard deviation of the FWHM of PSF and the effective resolution in the unit of pixel.

# of projection	FWHM of PSF	Effective resolution
1 (Cor.)	2.6±1.1 pixel	16.9±4.6 pixel
2 (Cor.+Sag.)	2.5±1.6 pixel	7.0±2.3 pixel
3 (Cor.+Sag.+Tra.)	1.4±0.5 pixel	4.7±1.6 pixel